PNAS RESEARCH ARTICLE | CHEMISTRY

Quenching singlet oxygen via intersystem crossing for a stable Li-O_2 battery

Zhuoliang Jiang[a], Yaohui Huang[a], Zhuo Zhu[a], Suning Gao[a], Qingliang Lv[a], and Fujun Li[a,b,1]

Edited by Alexis Bell, University of California, Berkeley, Berkeley, CA; received February 16, 2022; accepted July 07, 2022

Aprotic Li-O_2 batteries are a promising energy storage technology, however severe side reactions during cycles lead to their poor rechargeability. Herein, highly reactive singlet oxygen ($^1O_2$) is revealed to generate in both the discharging and charging processes and is deterimental to battery stability. Electron-rich triphenylamine (TPA) is demonstrated as an effective quencher in the electrolyte to mitigate $^1O_2$ and its associated parasitic reactions, which has the tertiary amine and phenyl groups to manifest excellent electrochemical stability and chemical reversibility. It reacts with electrophilic $^1O_2$ to form a singlet complex during cycles, and it then quickly transforms to a triplet complex through nonradiative intersystem crossing (ISC). This efficiently accelerates the conversion of $^1O_2$ to the ground-state triplet oxygen to eliminate its derived side reactions, and the regeneration of TPA. These enable the Li-O_2 battery with obviously reduced overvoltages and prolonged lifetime for over 310 cycles when coupled with a RuO_2 catalyst. This work highlights the ISC mechanism to quench $^1O_2$ in Li-O_2 battery.

Li-O_2 battery | singlet oxygen | triphenylamine | intersystem crossing mechanism | quencher

Aprotic Li-O_2 battery has gained extensive interests because of its high theoretical energy density of ~3,600 Wh kg^{-1} ($O_2 + 2Li + 2e^- \leftrightarrow Li_2O_2$, $E_0 = 2.96$ V vs. Li^+/Li), however, it is hampered by the irreversible parasitic reactions at cathodes, leading to large discharge/charge overvoltages and poor rechargeability (1–4). This necessitates adoption of efficient cathode catalysts and suppression of inferior side reactions; the former has aroused a lot of efforts in recent years, while the latter is ambiguous and cannot be fully clarified for a long time (5–9). Recently, highly reactive singlet oxygen ($^1O_2$, the first excitedstate of oxygen) was demonstrated as a crucially important cause for parasitic reactions in Li-O_2 batteries, which is mainly generated via the disproportionation of superoxide anion (O_2^-) and the oxidation of peroxide/superoxide species in the respective discharge and charge processes (10–14). The strong electrophilic $^1O_2$ easily attacks most of cell components, like the organic solvents, electrolyte salts, and electrodes, to yield passivating by-products and induce capacity decay and even premature battery death (15–18). It is imperative to eliminate the reactive $^1O_2$ and suppress the associated parasitic reactions for the development of reversible Li-O_2 batteries.

The feasible solutions to $^1O_2$ in aprotic Li-O_2 batteries involve the reduction of charge voltages and the usage of $^1O_2$ quenchers (10, 13, 15). The former is to lower the charge potentials below the equilibrium potential of $^1O_2$ (~3.55 V vs. Li^+/Li) to partially mitigate the formation of $^1O_2$, further improving the cycling stability of Li-O_2 battery (5, 19–21). Alternatively, electron-rich quenchers are able to accelerate the decay of $^1O_2$ to the ground-state triplet oxygen ($^3O_2$) and restrain the harmful $^1O_2$-related side reactions (22). However, most adopted quenchers, such as organic amines, radical molecules, and redox mediators (RMs), are limited by their electrochemical irreversibility, insufficient chemical stability and low quenching efficiencies (23). For instance, 1,4-diazabicyclo[2.2.2]octane (DABCO) and RM of 5,10-dimethylphenazine (DMPZ) have manifested modest quenching efficiencies, but they are hindered by the electrochemical irreversibility and moderate chemical stability against $^1O_2$, respectively (24–26). Exploration of effective and chemically/electrochemically stable quenchers to scavenge $^1O_2$ remains quite challenging for Li-O_2 batteries. Furthermore, the quenching mechanism for the decay of $^1O_2$ has seldom been studied and urgently needs to be unveiled.

Herein, we report an electron-rich and robust triphenylamine (TPA) as the $^1O_2$ quencher for Li-O_2 batteries, which is generated in both the discharge and charge processes. The TPA quencher features as excellent electrochemical and chemical reversibility against $^1O_2$. The elimination of $^1O_2$ and suppression of its associated parasitic reactions are confirmed by in-situ UV-visible absorption spectroscopy, ^1H NMR, and differential electrochemical mass spectrometry. During discharge and charge, TPA combines with electrophilic $^1O_2$ to form a singlet complex, which rapidly converts to a triplet complex

Significance

The demand for electric vehicles with long driving range requires energy storage technology beyond Li-ion batteries. Aprotic Li-O_2 batteries with high theoretical energy density have attracted significant interest as a potential alternative, but severe side reactions, especially singlet oxygen ($^1O_2$) and its related reactions, induce capacity decay and shorten the lifespan for Li-O_2 batteries, which is also challenging for Li-rich materials. Although quenchers have been attempted to suppress $^1O_2$, the reaction mechanism is ambiguous, which is important for rational design of quenchers. Here, an electrochemically stable and chemically reversible triphenylamine is demonstrated to be an efficient quencher to suppress $^1O_2$ via nonradiative intersystem crossing and hence its associated side reactions, and then it significantly prolongs the lifetime for Li-O_2 batteries.

Author affiliations: [a]Key Laboratory of Advanced Energy Materials Chemistry (Ministry of Education), Renewable Energy Conversion and Storage Center (RECAST), College of Chemistry, Nankai University, Tianjin, 300071, China; and [b]Haihe Laboratory of Sustainable Chemical Transformations, Tianjin 300192, China

Author contributions: F.L. designed research; Z.J. and Y.H. performed research; Z.J., S.G., and Q.L. analyzed data; and Z.J., Z.Z., and F.L. wrote the paper.

The authors declare no competing interest.

This article is a PNAS Direct Submission.

[1]To whom correspondence may be addressed. Email: fujunli@nankai.edu.cn.

This article contains supporting information online at http://www.pnas.org/lookup/suppl/doi:10.1073/pnas.2202835119/-/DCSupplemental.

Published August 15, 2022.

via radiationless intersystem crossing (ISC), accompanied with the transformation of $^1O_2$ to $^3O_2$ and regeneration of TPA. It effectively hinders the $^1O_2$-driven parasitic reactions and rewards the Li-O_2 battery with reduced discharge/charge voltage gaps and prolonged lifespan. This work provides insights into the design of efficient and stable $^1O_2$ quenchers for long cycling Li-O_2 batteries.

Results

Generation of $^1O_2$ During Discharge and Charge. The generation of $^1O_2$ during discharge and charge is primarily quantified by monitoring the concentration change of 9,10-dimethylanthracene (DMA) via in situ UV-visible (UV-vis) measurement. DMA is chosen as the $^1O_2$ probe because its absorbance of the characteristic peak at 379 nm is proportional to its concentration and decreases after selectively reacting with $^1O_2$ to form endoperoxide (DMA-O_2) (5), as confirmed by UV-vis and ^{1}H-NMR measurements (Fig. 1*A* and *SI Appendix*, Figs. S1–S5). For the in situ UV-vis measurements, the Li-O_2 battery is assembled inside a gas-tight quartz cuvette with an electrolyte of 50 μM DMA and 1.0 M lithium bis(trifluorosulfonyl)imide (LiTFSI) in diethylene glycol dimethyl ether (G2) solvent. Fig. 1*B* presents the discharge/charge profile and the corresponding DMA concentration changes of a Super P (SP)-based Li-O_2 battery. During discharge, the DMA concentration maintains roughly constant at 50 μM within the detection accuracy of the UV-vis instrument. Alternatively, high-performance liquid chromatography coupled with mass spectrometry (HPLC-MS) is applied to detect the conversion of DMA to DMA-O_2 after discharging a SP-based Li-O_2 battery to 1 mAh in Fig. 1*C*, in which a high concentration of 30 mM DMA is added in the electrolyte to guarantee adequate capture of $^1O_2$. The blue curve of initial electrolyte reveals the existence of DMA, and the red profile of discharged electrolyte presents a prominent peak of DMA and a small peak of DMA-O_2. This suggests a tiny amount of $^1O_2$ generated during discharge.

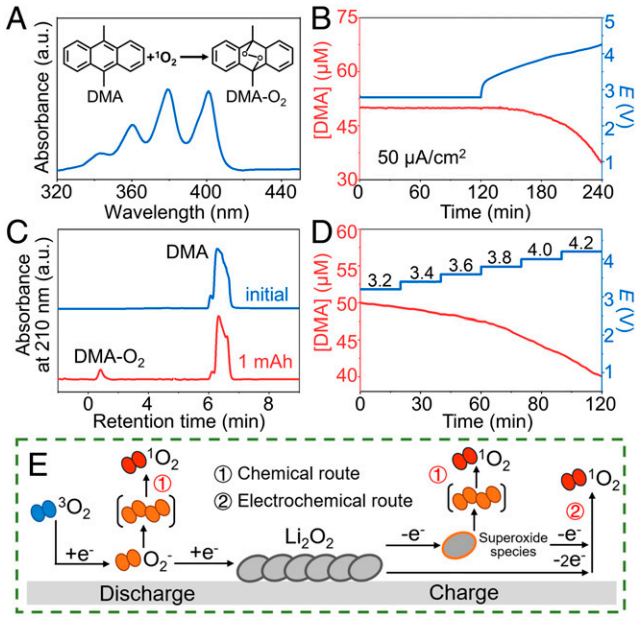

Fig. 1. (*A*) UV-vis absorption spectrum of DMA in G2 electrolyte. The embedded equation shows the addition reaction of DMA and $^1O_2$. (*B*) Discharge/charge profile of a SP-based Li-O_2 battery and the corresponding DMA concentration changes. (*C*) HPLC-MS analyses of initial electrolyte and the electrolyte after discharged to 1 mAh. (*D*) DMA consumption profile of a SP-based Li-O_2 battery charged at different voltage plateaus. (*E*) Schematic generation of $^1O_2$ during discharging and charging.

When the SP-based Li-O_2 battery is charged in Fig. 1*B*, the DMA concentration decreases constantly from the beginning to the end of charge, indicating that $^1O_2$ is mainly generated in the charging process. The calculated $^1O_2$ yield of 15.1 μM is corresponding to a $^1O_2/O_2$ ratio of ∼2.1%, in agreement with the previous report (5). The $^1O_2$ generation rate profile is obtained by taking the derivative of DMA consumption (*SI Appendix*, Fig. S6), revealing that the $^1O_2$ generation increases with the rising charge voltage. It is further verified by a voltage-step charging test in Fig. 1*D*, in which a predischarged Li-O_2 battery is gradually charged at each varied voltage from 3.2 to 4.2 V for 20 min. It is found that DMA is slowly consumed from 50.0 to 48.4 μM when charged at low plateaus of 3.2 V and 3.4 V. However, the DMA concentration is promptly reduced to 40.0 μM when the charge plateau surpasses the equilibrium potential of $^1O_2$ (∼3.55 V), from 3.6 to 4.2 V. When controlling the charge voltages below ∼3.6 V by employing a RuO_2 catalyst (*SI Appendix*, Figs. S7 and S8), the $^1O_2$ yield of Li-O_2 battery is decreased to 9.5 μM (*SI Appendix*, Fig. S6). These imply that the generation of $^1O_2$ is promoted by high charge voltages.

Fig. 1*E* illustrates the chemical and electrochemical generation routes of $^1O_2$ in the discharging and charging processes of a Li-O_2 battery. During discharge, $^3O_2$ is firstly reduced to O_2^- anion via one-electron process, and then Li^+ induces the disproportionation of O_2^- in the electrolyte for the formation of either $^3O_2$ or $^1O_2$, denoted as the chemical $^1O_2$ generation route. This process is more thermodynamically favorable to form the ground-state $^3O_2$ as product rather than the excited-state $^1O_2$, leading to a tiny amount of $^1O_2$ generated during discharge, as confirmed in Fig. 1 *B* and *C*. Upon charging, the discharge product of Li_2O_2 is initially oxidized to superoxide species, like O_2^- and Li-deficient $Li_{2-x}O_2$, and the soluble part is slightly converted to $^1O_2$ via the chemical route in the whole charging process. The further electrochemical oxidation of peroxide and superoxide species mostly evolves $^3O_2$ under low charge voltages, so only a small amount of $^1O_2$ is generated at the beginning of charge. However, the formation of $^1O_2$ becomes thermodynamically favorable when the charge voltage surpasses the equilibrium potential of $^1O_2$ (∼3.55 V), resulting in the generation of massive $^1O_2$ from the middle to the end of charge, denoted as the electrochemical $^1O_2$ generation route.

Suppression of $^1O_2$ and Associated Parasitic Reactions. $^1O_2$ with a fully occupied and an empty π* orbitals is highly electrophilic, and can be accepted by electron-rich molecules or groups (21, 22). Tertiary amine with three phenyl groups, namely TPA, is used as the quencher to suppress $^1O_2$ and its derived side reactions for Li-O_2 battery, as depicted in Fig. 2*A*. TPA has been widely used as electrode material because of its electrochemical reversibility and chemical stability against various reactive oxygen species (ROS) in the absence of active hydrogen atoms (17, 27, 28). The cyclic voltammetry (CV) curve in Fig. 2*A* shows the reversible redox behavior of TPA^+/TPA, and indicates its excellent electrochemical stability compared with the unstable DABCO (*SI Appendix*, Figs. S9 and S10). The ^{1}H-NMR spectra of TPA reveal its chemical stability against multiple ROS (including $^1O_2$, O_2^-, Li_2O_2, and O_2) and Li metal (Fig. 2*B* and *SI Appendix*, Figs. S11 and S12). The quenching effect of TPA is firstly verified in an external confirmatory test, where $^1O_2$ is generated through the disproportionation of O_2^- driven by Li^+. DMA is quickly consumed from 50.0 to 36.6 μM in the blank counterpart, while its concentration remains almost unchanged after addition of an optimized concentration of 10 mM TPA (*SI Appendix*, Figs. S13–S15). This results in its high $^1O_2$

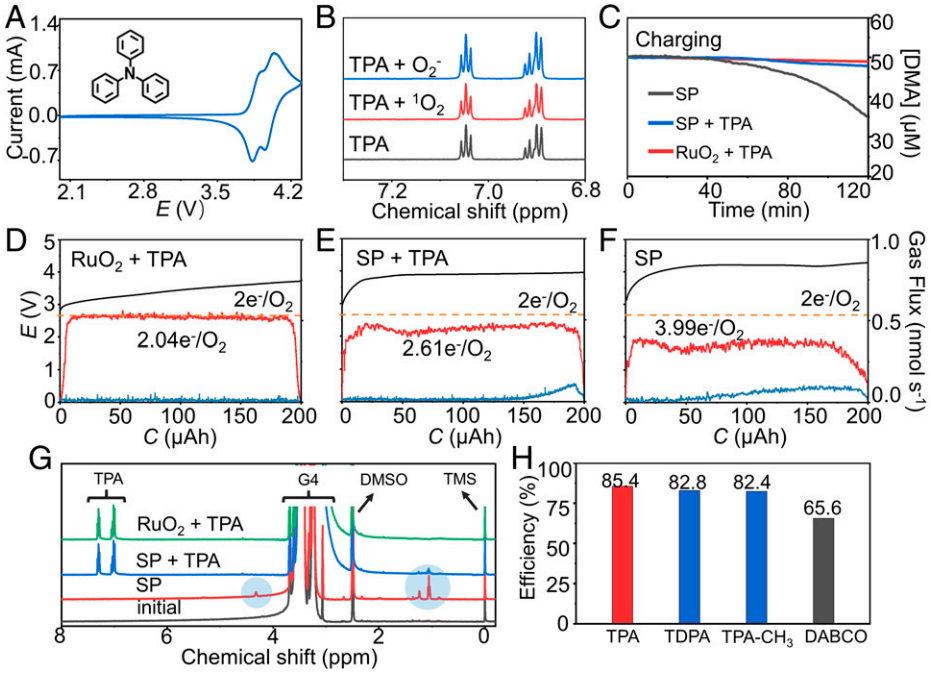

Fig. 2. (*A*) CV profile of TPA under Ar atmosphere. (*B*) Stability of TPA against O_2^- and $^1O_2$. (*C*) DMA concentration profiles in charging with SP or RuO_2 cathode and TPA. (*D–F*) Gas evolution during charging with RuO_2 + TPA, SP + TPA, and SP. Red and blue curves represent the respective evolution rates of O_2 and CO_2. (*G*) ^{1}H-NMR spectra of the electrolytes at the initial state and after 10 cycles in DMSO-d^6. (*H*) Quenching efficiencies of electron-rich TPA analogs.

quenching efficiency of 99.3%, as compared with 83.2% of DABCO based on the equation (*SI Appendix*, Fig. S16). The quenching effect of TPA in Li-O_2 battery is evaluated by monitoring the DMA concentration change during charge, since the tiny generation of $^1O_2$ during discharge is below the detection limit, as revealed in Fig. 1*B*. When TPA is used as an electrolyte additive in the SP-based Li-O_2 battery, the DMA concentration is close to 50 μM with tiny consumption at the end of charge in Fig. 2*C*, and it leads to low $^1O_2$ yield of 2.2 μM and high $^1O_2$ quenching efficiency of 85.4% (*SI Appendix*, Fig. S16). The quenching efficiency can be further improved to 94.8% by replacing SP with the RuO_2 catalyst, which mitigates the generation of $^1O_2$ via reducing charge voltages (*SI Appendix*, Fig. S6).

The gas evolution of Li-O_2 battery is detected by differential electrochemical mass spectrometry (DEMS) measurement in charging processes. In Fig. 2*D*, only O_2 is evolved in the TPA-mediated Li-O_2 battery with the RuO_2 catalyst (denoted as RuO_2 + TPA), and no other gases like CO_2 and H_2 are detected. The gas flux of O_2 approaches to the theoretical value in the whole charging process, resulting in a remarkable charge-to-O_2 ratio of 2.04 e^-/O_2. The high reversibility is originated from the effective prevention of $^1O_2$, high voltages, and the related parasitic reactions with the combination of TPA and RuO_2 catalyst. For the TPA-mediated Li-O_2 battery with SP catalyst (denoted as SP + TPA) in Fig. 2*E* or the TPA-free Li-O_2 battery with RuO_2 catalyst (*SI Appendix*, Fig. S17), they present good reversibility with charge-to-O_2 ratios of 2.61 and 2.41 e^-/O_2, respectively, in which TPA can suppress $^1O_2$ and RuO_2 contributes to reducing the charge voltages. The residual parasitic reactions lead to small amount of CO_2 evolution at the end of charge. In Fig. 2*F*, the charge voltage easily reaches up to 4.2 V in the TPA-free Li-O_2 battery with SP catalyst, which accelerates the generation of $^1O_2$ as revealed by UV-vis analyses. The formation of $^1O_2$ and high charge voltages induce severe side reactions, resulting in a high charge-to-O_2 ratio of 3.39 e^-/O_2, massive CO_2 release during charge, as well as the inferior stability of Li-O_2 battery.

The stabilities of electrolytes are analyzed by monitoring the signals of byproducts via ^{1}H-NMR measurements. The NMR spectrum of initial electrolyte in Fig. 2*G* displays prominent peaks of tetraethylene glycol dimethyl ether (G4), dimethyl sulfoxide (DMSO), and tetramethylsilane (TMS), which are originated from electrolyte solvent of distilled G4 and DMSO-d^6 deuterated reagent, respectively. For the TPA-mediated Li-O_2 battery with RuO_2 catalyst, the NMR spectra display no impurity peaks after ten cycles and minimal byproducts after one hundred cycles (Fig. 2*G* and *SI Appendix*, Fig. S18). This proves the long-term stability of TPA and the successful suppression of electrolyte degradation by preventing $^1O_2$, high voltages, and the associated parasitic reactions, as confirmed by DEMS results. In sharp contrast, a number of distinctive peaks associated with alkyls and hydroxyls of carboxylates appear in the NMR spectra of the TPA-free counterparts with SP and RuO_2 catalysts after 10 cycles, and become pronounced after 100 cycles (Fig. 2*G* and *SI Appendix*, Fig. S18). These electrolyte counterparts are relatively stable after 1 cycle (*SI Appendix*, Figs. S18 and S19), however, the hazards of $^1O_2$-induced parasitic reactions accumulate during cycling and gradually induce the instability of Li-O_2 battery. The blue profile of TPA-mediated Li-O_2 battery with SP catalyst represents minor signals of byproducts, suggesting inhibition of the $^1O_2$-driven side reactions. These reveal that TPA can efficiently eliminate $^1O_2$ and relevant side reactions.

Two electron-rich TPA analogs, such as Tris[4-(diethylamino)phenyl]amine (TDPA) and 4,4',4''-trimethyltriphenylamine (TPA-CH_3), are also selected as potential quenchers for Li-O_2 battery (*SI Appendix*, Fig. S20). The CV curves of TDPA and TPA-CH_3 reveal their electrochemical reversibility in the operating voltage window of Li-O_2 battery (*SI Appendix*, Figs. S21 and S22). The quenching effects of TDPA and TPA-CH_3 for $^1O_2$ in SP-based Li-O_2 batteries are measured via in situ UV-vis and HPLC-MS analyses (*SI Appendix*, Figs. S23–S25) and compared with TPA as well as DABCO in Fig. 2*H*. TPA shows the highest quenching efficiency of 85.4%, against 82.8% and 82.4% of TDPA and TPA-CH_3, respectively. Both

TDPA and TPA-CH_3 possess excellent quenching effect, mainly because of the robust and electron-rich structure of tertiary amine with three phenyl groups. Conversely, the unsatisfactory chemical stability of DABCO limits its quenching effect in battery systems (23, 24), resulting in low quenching efficiency of 65.6%. In general, robust and electron-rich chemicals own universal $^1O_2$ quenching effect for Li-O_2 battery.

Electrochemical Performance. The charge voltage of SP-based battery surpasses 4.0 V with or without TPA (*SI Appendix*, Figs. S26 and S27), resulting in serious electrolyte degradation as demonstrated in Fig. 2*G*. RuO_2 is introduced as cathode catalyst to accelerate the decomposition of Li_2O_2 and reduce the charge voltages for Li-O_2 battery. The cycling performance of RuO_2-based Li-O_2 batteries with and without TPA is displayed in Fig. 3 *A* and *B* with a fixed capacity of 1000 mAh g^{-1} at 500 mA g^{-1}. Both the Li-O_2 batteries with and without TPA present small discharge/charge voltage gaps of ~0.92 V for the first 5 cycles. In the TPA-mediated battery, it can be continuously discharged and charged for 310 cycles with little deterioration of discharge and charge polarization, indicating excellent cycling stability. The terminal charge voltage remains below 3.90 V after 300 cycles to exclude oxidation of TPA. Accordingly, the reversible formation and decomposition of toroidal Li_2O_2 are also verified by X-ray diffraction (XRD), Raman spectra and scanning electron microscopy (SEM) images (*SI Appendix*, Figs. S28–S30), respectively. In contrast, the discharge/charge plateaus of TPA-free battery present increasing voltage gaps of ~1.14 V after 20 cycles, due to the accumulation of $^1O_2$-driven parasitic reactions, as confirmed by DEMS and ^{1}H-NMR analyses (*SI Appendix*, Figs. S17 and S18). It can only maintain for 150 cycles with the terminal discharge voltage quickly dropping to 2.2 V in Fig. 3*C*. The superior cycle stability of TPA-mediated battery is ascribed to the elimination of harmful $^1O_2$ and its derived reactions at low charge voltages, however the degradation of Li anode also impairs the cycle stability and shortens the operation time to some extent (as discussed in *SI Appendix*, Fig. S31).

Quenching Reaction Mechanism. The Gibbs free energy diagram in Fig. 4*A* illustrates the quenching process, and the interaction region indicator (IRI) analysis in Fig. 4*B* visualizes the interaction between TPA and $^1O_2$ during quenching. After the chemical or electrochemical generation of $^1O_2$ during cycling, electrophilic $^1O_2$ is firstly adsorbed at the phenyl group of TPA via weak attraction as shown in Fig. 4*B* and forms encounter complex (denoted as EC). It is prone to converting to singlet charge-transfer complex (denoted as 1CT), rather than to undergo endothermic addition reaction and form a byproduct of endoperoxide, in line with NMR spectra in Fig. 2*B*. Based on the Gibbs free energy diagram in Fig. 4*A*, 1CT with high Gibbs free energy of 0.99 eV spontaneously decays to triplet charge-transfer complex (3CT) with low Gibbs free energy of -0.78 eV through ISC mechanism, accompanied with the release of heat energy to the environment. The optimized structure of 3CT indicates that the oxygen in 3CT is changed from $^1O_2$ to $^3O_2$ after ISC. Because of the absence of electrophilicity for $^3O_2$, it interacts with TPA through weak Van der Waals force in Fig. 4*B*, and then $^3O_2$ easily dissociates from 3CT to the environment.

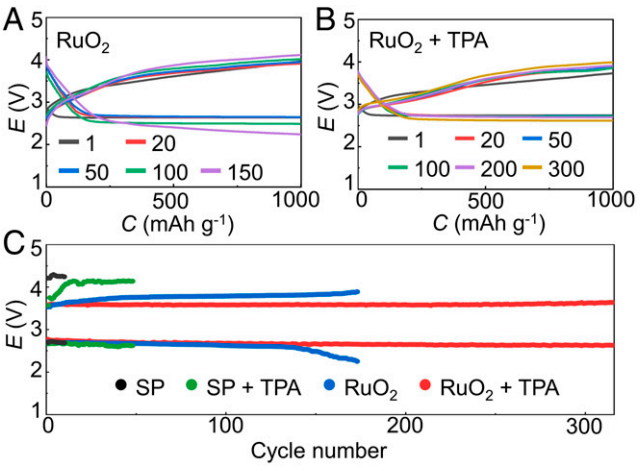

Fig. 3. (*A* and *B*) Discharge and charge profiles of the RuO_2-based Li-O_2 batteries with and without TPA at 500 mA g^{-1}. (*C*) Cycling performance of Li-O_2 batteries (*y* axis represents average discharge/charge voltage).

ISC is a nonradiative transition from singlet to triplet chemicals, accompanied with the release of energy and the transformation of multiplicity. The former has been revealed by the Gibbs free energy diagram in Fig. 4*A*, and the transformation from singlet to triplet state is illustrated in Fig. 4*C*. Both TPA and $^1O_2$ are spin singlet since all the electrons are spin-paired with opposite directions, leading to total spin (S) of 0 and then spin multiplicity (M = 2S + 1) of 1. When EC converts to 1CT, a spin-up electron (↑) from the P_z orbital of N atom in TPA transfers to the empty π^* orbital of $^1O_2$, between which strong attraction is present, as proven by IRI analysis, molecular orbital component, and Mulliken analyses (Fig. 4*B* and *SI Appendix*, Figs. S32 and S33 and Table S2), respectively. 1CT is spin singlet because the single electrons in the π^* orbital of $^1O_2$ and in the P_z orbital of N atom of TPA have opposite spin directions, leading to a total spin of 0. Along with the release of energy during ISC, a spin-down electron (↓) in the fully occupied π^* orbital of $^1O_2$ in 1CT transfers back to the central N atom of TPA (*SI Appendix*, Fig. S32) and undergoes spin-flip and fills the spin-up vacancy in the P_z orbital of N atom, due to Pauli exclusion principle, with formation of triplet 3CT. The electronic structure of 3CT in Fig. 4*C* indicates that the oxygen is transformed from $^1O_2$ to $^3O_2$ after ISC, with two spin-up electrons occupying two different π^* orbitals. Finally, $^3O_2$ and TPA are dissociated from 3CT, and TPA participates another quenching process. Fig. 4*D* exhibits the decay of $^1O_2$ to $^3O_2$ without or with TPA quencher. Generally, $^1O_2$ decays slowly to $^3O_2$ via a radiative transition mechanism (denoted as RT) with light emission, since the direct ISC from $^1O_2$ to $^3O_2$ is inhibited (21, 22). After introduction of TPA as a $^1O_2$ quencher, it interacts with $^1O_2$ to form 1CT and relaxes to 3CT through quick nonradiative ISC, with release of $^3O_2$. Therefore, TPA can greatly expedite the decay of $^1O_2$ to $^3O_2$ and mitigate the $^1O_2$-driven side reactions for stable and prolonged Li-O_2 battery.

Discussion

In summary, electron-rich TPA is demonstrated to be an efficient quencher to eliminate $^1O_2$ and the relevant side reactions in Li-O_2 battery. The robust tertiary amine and phenyl groups in TPA ensures its electrochemical reversibility and chemical stability against diverse ROS, as verified by CV and ^{1}H-NMR measurements. The electron-rich TPA can interact with electrophilic $^1O_2$ to form 1CT by transferring a spin-up electron (↑) from N atom of TPA to $^1O_2$. Then, 1CT quickly decays to 3CT through ISC mechanism, and simultaneously heat energy is released to the environment and a spin-down electron (↓) in $^1O_2$ undergoes spin-flip and transfers back to the central N atom of TPA. This accelerates the relaxing of $^1O_2$ and efficiently

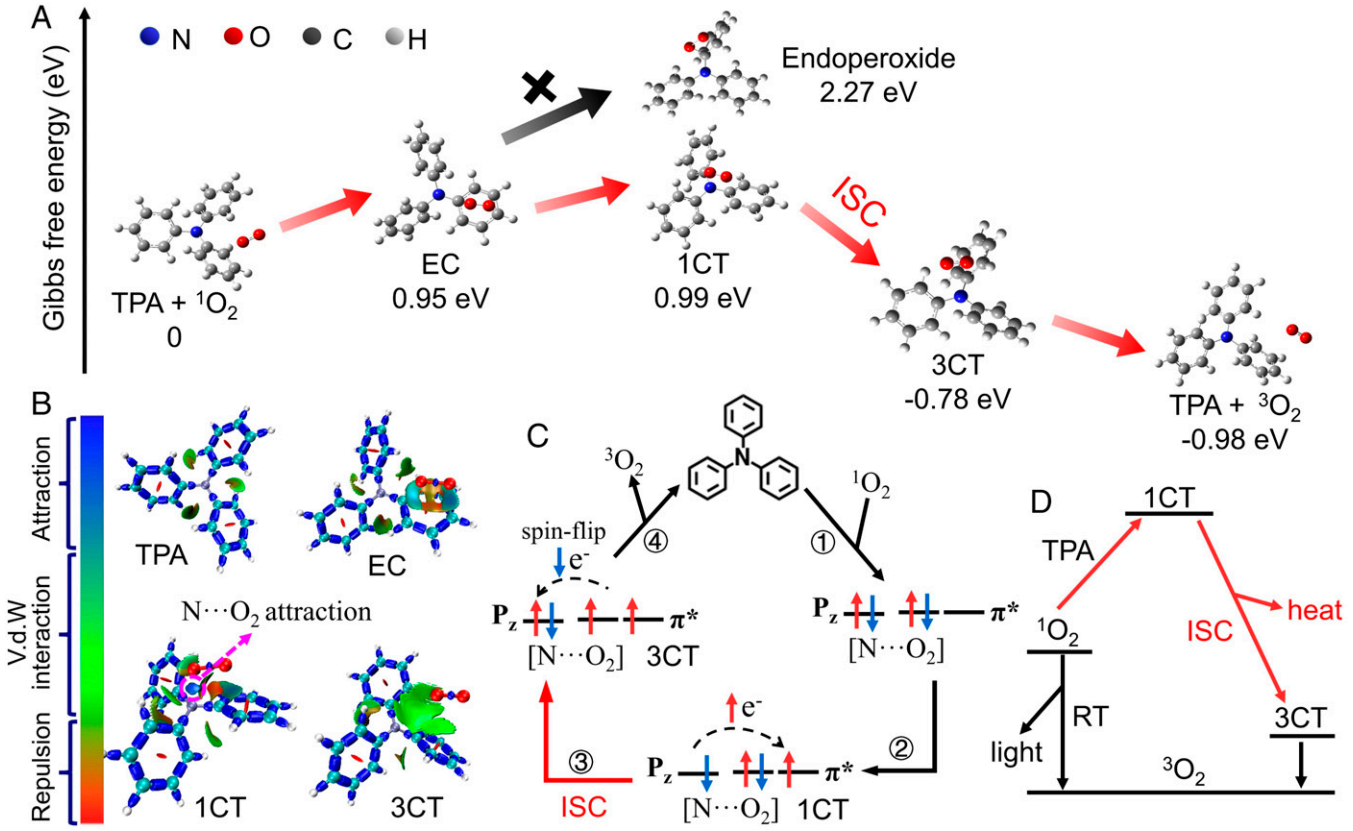

Fig. 4. (*A*) Gibbs free energy diagram of quenching process. Intermediate complex EC, 1CT and 3CT are encounter complex, singlet charge-transfer complex, and triplet charge-transfer complex, respectively. Endoperoxide is a possible by-product of $^1O_2$ and phenyl. (*B*) IRI analyses of intermediates during quenching. Red, green, and blue regions represent repulsion, Van der Waals interaction, and attraction, respectively. (*C*) Schematic diagram of conversion of spin state during ISC. Red and blue arrows represent spin-up and spin-down electrons, respectively. (*D*) Decay of $^1O_2$ with or without TPA.

restrains O_2-driven side reactions. Coupled with RuO_2 to reduce charge voltages and mitigate the generation of $^1O_2$, the TPA-mediated Li-O_2 battery exhibits superior reversibility of 2.04 e^-/O_2 during charge, reduced discharge/charge overvoltages and prolonged lifespan of 310 cycles. In addition, two electron-rich and robust TPA analogs of TDPA and TPA-CH_3 also demonstrate their universal $^1O_2$ quenching effect for Li-O_2 battery. This work highlights the vital role of ISC to quench $^1O_2$ and provides insights into the qualified quenchers for durable Li-O_2 battery.

Materials and Methods

Materials. All chemicals were stored in an argon-filled glovebox. G2 and G4 were distilled and kept with activated molecular sieves. LiTFSI was dried under vacuum for 12 h at 80 °C. DMA and KO_2 were directly used without further treatment. A series of $^1O_2$ quenchers such as TPA, DABCO, TPA-CH_3, and TDPA were dried under vacuum before use. RuO_2 catalyst was synthesized via precipitation reaction and calcination process (29). Carbon nanotube (denoted as CNT) was pretreated with nitric acid at 110 °C for 4 h, and then washed with ultrapure water and ethanol. One hundred milligrams of CNT and 200 mg $RuCl_3$ were dispersed in 30 mL ultrapure water by stirring for 30 min, into which a 0.2 M $NaHCO_3$ aqueous solution was added drop by drop until the pH reached 7. After stirring for 10 h, the sediment was washed with ultrapure water and ethanol, dried at 80 °C for 6 h and calcined at 150 °C for 4 h. The black powder was collected and denoted as RuO_2.

Material Characterization. SEM (JEOL-JSM7500F) was utilized to study the morphology of discharged products. XRD (Rigaku MiniFlex600) and Raman spectroscopy (LabRAM HR800 with a 532 nm laser) were applied to confirm the formation and decomposition of discharged products. The electrodes for the tests were washed with distilled DMA, dried under vacuum to remove residual solvents, and characterized under argon protection. UV-vis absorption spectra (Agilent Cary 60) were conducted to record the generation of $^1O_2$. ^{1}H-NMR (Bruker, 400 MHz) was operated to check electrolyte decomposition. Transmission electron microscopy (TEM; FEI Talos F200X G2) was utilized to characterize the RuO_2 catalyst. EPR spectrometer (Bruker, E580) is utilized to optimize the concentration of TPA.

Electrochemical Measurements. RuO_2 catalyst or SP was dispersed in ethanol solution by sonication with 10 w% sodium carboxymethylcellulose as the binder. The black suspension was sprayed on carbon cloth with a mass loading of ~0.3 mg cm^{-2}. The prepared carbon cloth was cut into discs (Φ10 mm) and dried in vacuum. The electrolyte was prepared by dissolving 1.0 M LiTFSI in G4. The electrolyte with $^1O_2$ quencher was prepared by adding extra 10 mM TPA or other quenchers. The Li-O_2 batteries were assembled in top-holed CR2032 coin cells in an argon-filled glovebox. Each cell contained a piece of Li foil (Φ10 mm), a glassy fiber separator (Φ16 mm) with 60 μL of electrolyte, and a catalyst-loaded carbon cathode (Φ10 mm). Galvanostatic cycling tests were run on Land battery instrument (CT2001A). CV measurement was performed on a Solartron 1470E electrochemical workstation.

In-situ DEMS measurement. DEMS measurement was conducted on a customized QMG250M1 commercial instrument from Linglu Instruments (Shanghai) Co., Ltd. Modified Swagelok-type Li-O_2 cells were used for DEMS measurement. Each cell contained a piece of Li foil (Φ14 mm), a glassy fiber separator (Φ22 mm) with 40 μL of G4 electrolyte, and a catalyst-loaded carbon cathode (Φ14 mm) with loading density of 0.5 mg cm^{-2}. The cell was discharged to 200 μAh before DEMS testing, then linked to a mass spectrometer by a gas-purging system and charged to 200 μAh at 100 μA. The flow rate of carrier gas (Ar) was set at 1 mL min^{-1}. The evolution of O_2 and CO_2 was monitored by the mass spectrometer during charge.

In situ and Ex situ $^1O_2$ Detection. In situ UV-vis tests were conducted using a UV-vis spectrophotometer. The generation of $^1O_2$ and quenching efficiency of

different additives were detected by measuring the decay of DMA concentration. A 1 cm high-precision quartz cell with a custom-made gasproof polytetrafluoroethylene (PTFE) lid was used for the in situ UV-vis test. The cell contained a catalyst-loaded carbon cathode, a piece of Li foil as an anode, and a 1.2 mL G2 electrolyte with or without 10 mM of $^1O_2$ quenchers. Before testing, O_2 was bubbled into the electrolyte for 20 min. The DMA concentration of 50 μM was chosen to balance effective trapping concentration of DMA and excellent detecting precision of the instrument. For in situ UV-vis tests, the cells were discharged and charged under 50 μA cm^{-2} for 2 h, respectively.

HPLC-MS was utilized to analyze the transformation of DMA to DMA-O_2, with 30 mM DMA in the electrolyte to guarantee enhanced sensitivity. The electrolyte was extracted from the separator and cathode of each cell using 200 μL DME. Then the DME solution was evaporated under vacuum. After dissolving the residue in 10 μL DME, a volume of 2 μL was injected into the HPLC-MS equipment. The DMA to DMA-O_2 conversion was measured from the absorbance at 210 nm.

DFT Calculations. Dispersion-corrected density functional theory calculations (DFT-D3) was performed by using Gaussian 16 software package (30, 31). Molecule structures were relaxed with Becky three parameter exchange function and Lee-Yang-Parr correlation functional (B3LYP) with 6-31+G (d,p) basis set (32–34). Vibrational frequency analyses were applied to ensure that the geometry optimization was at local minima and to determine the zero-point energies. The electronic ground state energy of complex was obtained at M06-2X level with 6-311+G (d,p) basis set (35). Thermal correction to Gibbs free energy was acquired from vibrational frequency calculations using B3LYP with 6-31+G (d,p) basis set. In this case of DFT energy calculation, the correction of $^1O_2$ was 0.98 eV (16). The implicit solvation model based on density models was utilized to model solvent effects (eps = 7.68, epsinf = 1.432). IRI analysis revealing chemical bonding and weak interaction region, and natural atomic orbital analysis showing the contribution of each atom in orbitals based on DFT results were conducted by Multiwfn package (36, 37).

Data, Materials, and Software Availability. All study data are included in the article and/or supporting information.

ACKNOWLEDGMENTS. This work was supported by the Ministry of Science and Technology of China (2017YFA0206700), National Natural Science Foundation of China (51671107), Tianjin Natural Science Foundation (grant No. 19JCJQJC62400), the 111 project of B12015, and the Haihe Laboratory of Sustainable Chemical Transformations.

1. T. Liu *et al.*, Current challenges and routes forward for nonaqueous lithium-air batteries. *Chem. Rev.* **120**, 6558–6625 (2020).
2. W. J. Kwak *et al.*, Lithium-oxygen batteries and related systems: Potential, status, and future. *Chem. Rev.* **120**, 6626–6683 (2020).
3. C. Tan *et al.*, True reaction sites on discharge in Li-O_2 batteries. *J. Am. Chem. Soc.* **144**, 807–815 (2022).
4. J. Zhang *et al.*, A versatile functionalized ionic liquid to boost the solution-mediated performances of lithium-oxygen batteries. *Nat. Commun.* **10**, 602 (2019).
5. N. Mahne *et al.*, Singlet oxygen generation as a significant cause for parasitic reactions during cycling of aprotic lithium-oxygen batteries. *Nat. Energy* **2**, 17036 (2017).
6. Q. Lv, Z. Zhu, Y. Ni, J. Geng, F. Li, Spin-state manipulation of two-dimensional metal-organic framework with enhanced metal-oxygen covalency for lithium-oxygen batteries. *Angew. Chem. Int. Ed. Engl.* **61**, e202114293 (2022).
7. J. Zhang *et al.*, A long-life lithium-oxygen battery via a molecular qenching/mediating mechanism. *Sci. Adv.* **8**, eabm1899 (2022).
8. J. Zhang, B. Sun, Y. Zhao, K. Kretschmer, G. Wang, Modified tetrathiafulvalene as an organic conductor for improving performances of Li-O_2 batteries. *Angew. Chem. Int. Ed. Engl.* **56**, 8505–8509 (2017).
9. X. Li, R. X. Zhao, Y. Z. Fu, A. Manthiram, Nitrate additives for lithium batteries: Mechanisms, applications, and prospects. *eScience* **1**, 108–123 (2021).
10. J. Wandt, P. Jakes, J. Granwehr, H. A. Gasteiger, R. A. Eichel, Singlet oxygen formation during the charging process of an aprotic lithium-oxygen battery. *Angew. Chem. Int. Ed. Engl.* **55**, 6892–6895 (2016).
11. D. Córdoba, H. B. Rodríguez, E. J. Calvo, Singlet oxygen formation during the oxygen reduction reaction in DMSO LiTFSI on lithium air battery carbon electrodes. *ChemistrySelect* **4**, 12304–12307 (2019).
12. E. Mourad *et al.*, Singlet oxygen from cation driven superoxide disproportionation and consequences for aprotic Metal-O_2 batteries. *Energy Environ. Sci.* **12**, 2559–2568 (2019).
13. Y. K. Petit *et al.*, Mechanism of mediated alkali peroxide oxidation and triplet versus singlet oxygen formation. *Nat. Chem.* **13**, 465–471 (2021).
14. Y. Su, Z. Zhao, J. Huang, E. Wang, Z. Peng, Hunting the culprits: Reactive oxygen species in aprotic lithium-oxygen batteries. *J. Phys. Chem. C* **126**, 1243–1255 (2022).
15. J. W. Kwak *et al.*, Mutual conservation of redox mediator and singlet oxygen quencher in lithium-oxygen batteries. *ACS Catal.* **9**, 9914–9922 (2019).
16. J. W. Mullinax, C. W. Bauschlicher, Jr, J. W. Lawson, Reaction of singlet oxygen with the ethylene group: Implications for electrolyte stability in li-ion and Li-O_2 batteries. *J. Phys. Chem. A* **125**, 2876–2884 (2021).
17. Z. Huang *et al.*, A stable lithium-oxygen battery electrolyte based on fully methylated cyclic ether. *Angew. Chem. Int. Ed. Engl.* **58**, 2345–2349 (2019).
18. I. Ruiz de Larramendi, N. Ortiz-Vitoriano, Unraveling the effect of singlet oxygen on metal-O_2 batteries: Strategies toward deactivation. *Front Chem.* **8**, 605 (2020).
19. Q. Lv *et al.*, Semiconducting metal-organic polymer nanosheets for a photoinvolved Li-O_2 battery under visible light. *J. Am. Chem. Soc.* **143**, 1941–1947 (2021).
20. Z. Zhu *et al.*, Internal electric field and interfacial bonding engineered step-scheme junction for a visible-light-involved lithium-oxygen battery. *Angew. Chem. Int. Ed. Engl.* **61**, e202116699 (2022).
21. A. Schürmann, B. Luerßen, D. Mollenhauer, J. Janek, D. Schröder, Singlet oxygen in electrochemical cells: A critical review of literature and theory. *Chem. Rev.* **121**, 12445–12464 (2021).
22. C. Schweitzer, R. Schmidt, Physical mechanisms of generation and deactivation of singlet oxygen. *Chem. Rev.* **103**, 1685–1757 (2003).
23. H. W. Lee, H. Kim, H. G. Jung, Y. K. Sun, W. J. Kwak, Ambilaterality of RM towards $^1O_2$ in Li-O_2 batteries: Trap and quencher. *Adv. Funct. Mater.* **31**, 2102442 (2021).
24. Y. K. Petit *et al.*, DABCOnium: An efficient and high-voltage stable singlet oxygen quencher for metal-O_2 cells. *Angew. Chem. Int. Ed. Engl.* **58**, 6535–6539 (2019).
25. W. J. Kwak *et al.*, Deactivation of redox mediators in lithium-oxygen batteries by singlet oxygen. *Nat. Commun.* **10**, 1380 (2019).
26. J. K. Feng, Y. L. Cao, X. P. Ai, H. X. Yang, Polytriphenylamine: A high power and high capacity cathode material for rechargeable lithium batteries. *J. Power Sources* **177**, 99–204 (2008).
27. C. Su, Y. P. Ye, X. D. Bu, L. H. Xu, C. Zhang, Preparation and properties of polytriphenylamine/multi-walled carbon nanotube composite as a cathode material for li-ion batteries. *Adv. Mat. Res.* **335**, 1512–1515 (2011).
28. M. Zhang *et al.*, Suppressing singlet oxygen generation in lithium-oxygen batteries with redox mediators. *Energy Environ. Sci.* **13**, 2870–2877 (2020).
29. Z. Jian, P. Liu, F. Li, P. He, H. Zhou, Ru-RuO_2/CNT hybrids as high-activity pH-universal electrocatalysts for water splitting within 0.73 V in an asymmetric-electrolyte electrolyzer. *Nano Energy* **61**, 576–583 (2019).
30. S. Ehrlich, J. Moellmann, W. Reckien, T. Bredow, S. Grimme, System-dependent dispersion coefficients for the DFT-D3 treatment of adsorption processes on ionic surfaces. *ChemPhysChem* **12**, 3414–3420 (2011).
31. M. J. Frisch *et al.*, *Gaussian 16, Revision A.03* (Gaussian, Inc., Wallingford, CT, 2016).
32. C. Lee, W. Yang, R. G. Parr, Development of the Colle-Salvetti correlation-energy formula into a functional of the electron density. *Phys. Rev. B Condens. Matter* **37**, 785–789 (1988).
33. A. D. Becke, A new mixing of Hartree-Fock and local density-functional theories. *J. Chem. Phys.* **98**, 1372–1377 (1993).
34. A. D. Becke, Density-functional exchange-energy approximation with correct asymptotic behavior. *Phys. Rev. A Gen. Phys.* **38**, 3098–3100 (1988).
35. Y. Zhao, D. G. Truhlar, Theor. The M06 suite of density functionals for main group thermochemistry, thermochemical kinetics, noncovalent interactions, excited states, and transition elements: Two new functionals and systematic testing of four M06-class functionals and 12 other functionals. *Theor. Chem. Acc.* **120**, 215–241 (2007).
36. T. Lu, Q. Chen, Interaction region indicator: A simple real space function clearly revealing both chemical bonds and weak interactions. *Chemistry-Methods* **1**, 231–239 (2021).
37. T. Lu, F. Chen, Multiwfn: A multifunctional wavefunction analyzer. *J. Comput. Chem.* **33**, 580–592 (2012).